J. Fluid Mech. (2010), *vol.* 649, *pp.* 45–68.
doi:10.1017/S0022112009993363

Water bells formed on the underside of a horizontal plate. Part 2. Theory

ELEANOR C. BUTTON[1], JOHN F. DAVIDSON[2], GRAEME J. JAMESON[3] AND JOHN E. SADER[1]†

[1]Department of Mathematics and Statistics, University of Melbourne, Victoria 3010, Australia

[2]Department of Chemical Engineering, University of Cambridge, Cambridge CB2 3RA, UK

[3]Centre for Multiphase Processes, University of Newcastle, Callaghan, New South Wales 2308, Australia

(Received 6 November 2008; revised 9 November 2009; accepted 9 November 2009)

In a companion paper (Part 1, Jameson *et al. J. Fluid Mech.* vol. 649, 2010, 19–43), the discovery of a new type of water bell was reported. When a vertical liquid jet impacts on the underside of a large horizontal plate, the resulting thin film spreads radially along the plate to an unspecified abrupt departure point, from whence it falls away from the plate of its own accord. The departure radius of the fluid from the plate is seen to depend strongly on the volumetric flow rate. The falling liquid may then coalesce to form a water bell. Here we present a theoretical analysis and explanation of this phenomenon. A force balance determining the maximum radial extension of the thin film flow along the plate is considered as a mechanism for fluid departure from the plate, for which an analytical model is developed. This model gives good predictions of the measured radius of departure. When a water bell has been formed, and the flow rate is altered, many interesting shapes are produced that depend on the shapes at previous flow rates. We discuss the origin of this hysteresis, and also present a leading order theory for the bell shape under a regime of changing flow rate. The models are compared with experimental results spanning two orders of magnitude in viscosity.

1. Introduction

A water bell is formed when an axisymmetric thin sheet of fluid falls under gravity, and closes to trap a volume of air. These water bells were first discovered by Felix Savart, in 1833, and interest has been revived many times up to the present day.

The discovery of a new water bell phenomenon is described in a companion paper (Part 1, Jameson *et al.* 2010). A liquid jet is fired upwards, and collides with the underside of a large horizontal plate. The liquid spreads radially in a thin layer on the underside of the plate, until it reaches an unspecified point, where it detaches from the surface and falls. After detachment, the liquid may fall in threads, or coalesce to form a water bell. When the liquid sheet stabilizes to form a bell, the shape can change dramatically as the flow rate of the impinging jet is varied. In some cases, the bells may have greater radial dimensions towards the bottom, making them unlike

† Email address for correspondence: jsader@unimelb.edu.au

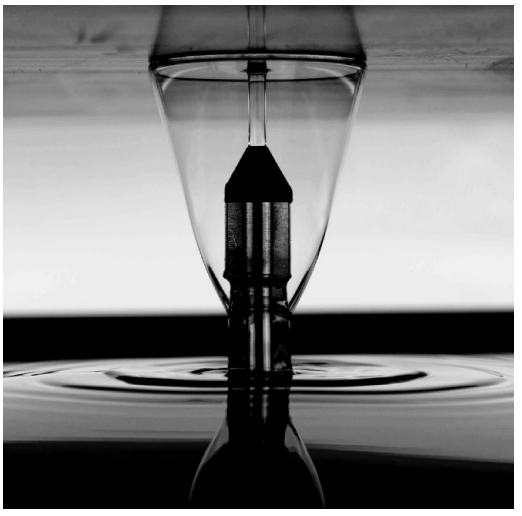

FIGURE 1. A water bell formed on the underside of a horizontal plate. This bell was formed using a 70 % glycerol mixture, pumped at a flow rate of 6.7 L min^{-1} through a jet of radius 4 mm onto a Teflon surface.

any water bells studied previously. An example of the jet impact, abrupt departure from the solid surface and water bell shape is shown in figure 1.

In previous work, a liquid jet is directed downwards at a small circular horizontal disk to form a water bell. The liquid spreads radially, and upon reaching the edge of the disk, it forms a free liquid film. Surface tension forces cause this falling film to close in on itself, trapping air inside and producing stable and interesting shapes. The existence of these bells was revealed by Savart (1833*b*), and since then there have been many contributions to their theory. Initial theories on the cohesion of liquids came from Boussinesq (1869*a*,*b*), the latter work containing the first theoretical analysis of water bells. Boussinesq balanced inertial forces with the forces of surface tension and gravity to produce a governing equation for the shape of such a bell. Inspired by the experimental work of Hopwood (1952), a further mathematical formulation was sought by Lance & Perry (1953). A modified Boussinesq equation was solved numerically, for particular parameter values. By investigating a pressure difference across the liquid film, shapes were produced that closely resembled the experiments.

The governing equation was then non-dimensionalized by Taylor (1959*a*), who noticed that the shape of the bell was determined by only two parameters; one of the terms containing gravity, and the other the pressure difference. In the case of both these mechanisms being negligible, the solution reduces to a catenary. Benedetto & Caglioti (1998) also derived this shape using the method of stationary action. Detailed study into the dependence of gravity was conducted by Dumbleton (1969), and into internal air circulation by Wegener & Parlange (1964) and Parlange (1967). Theoretical work on the breakup of liquid sheets was conducted by Taylor (1959*c*), Culick (1960), Brenner & Gueyffier (1999) and Clanet & Villermaux (2002), while the stability of water bells themselves was studied in detail by Clanet (2001). Other types of water bells have been studied including swirling bells (Bark *et al.* 1979; Gasser & Marty 1994), reverse water bells (Engel 1966; Thoroddsen 2002; Clanet 2007), transonic water bells (Brunet, Clanet & Limat 2004), annular liquid curtains (Jeandel & Dumouchel 1999; Pirat *et al.* 2006) and polygonal water bells (Aristoff *et al.* 2006).

In this paper, a theoretical model is presented for water bells formed on the underside of an effectively infinite horizontal plate, as reported in Part 1. The flow along the underside of the plate is considered separately to the falling film. The independence of these two aspects of the flow is discussed. The approach of Watson (1964) to the flow preceding a circular hydraulic jump is recalled in detail. A force balance is used to determine the maximum radial extension of the thin film on the underside of the plate; this is considered as a mechanism for determining the detachment radius. Both laminar and turbulent flows are examined theoretically. The shape of the falling film is then calculated, and connected with the top flow to create a self-consistent theoretical model. Finally, all results are compared with experiments in § 3.

2. Theory

Initial measurements indicate that the departure radius of the liquid from the plate depends strongly on the flow rate of the impinging jet, but not on the shape of the water bell itself. One particular experiment, described in detail in the companion paper, is of importance in justifying the separation of analysis for the top flow and the falling sheet. A water bell was formed at a constant flow rate, and air was added to the inside of the bell using a special attachment to the nozzle. This acted to change the shape of the water bell. The bell increased in size as air was added, and the water bell departure angle changed substantially. Despite these transformations, the departure radius remained constant. This leads to the important conclusion that the water bell departure angle does not have a significant influence on the departure radius. Strong hysteresis was observed in the water bell shape, when the flow rate was altered from that of the initial bell formation. These hysteretic effects caused the departure radius to change by less than 10 % for a given flow rate, and are considered to be of secondary importance to its determination. Distinct theories are thus developed for the departure radius and bell shape.

2.1. *Departure radius*

Disintegration of a radially expanding fluid sheet has been discussed previously for sheets formed by the impact of two co-axial jets (Savart 1833*a*), by a single jet impinging normally on a small finite disk to form a free moving film (Taylor 1959*c*) and by drops impacting on small targets (Rozhkov, Prunet-Foch & Vignes-Adler 2002). In these cases, flow in the horizontal film may be considered inviscid, and Taylor (1959*c*) provided a condition that must be satisfied at the radius of disintegration. Taylor considered a sheet of uniform thickness, and constructed a theory requiring a force balance along a radial line, where force (per unit length) due to surface tension at the edge of the film opposes the expansion. Should the fluid momentum flux be greater than the surface tension force, the expansion will continue; otherwise the rim of the sheet must contract. Equilibrium is achieved when these two forces are equal. Using this argument Taylor showed that the film disintegrates when

$$2\gamma = \rho h U^2, \tag{2.1}$$

where γ is the surface tension, ρ the density, h the thickness of the film and U is the velocity at the breakup point. Clanet & Villermaux (2002) formally showed an identical result holds for films of uniform velocity and varying thickness.

This idea is now extended to the present problem: a thin film spreading on the underside of a horizontal plate (see figure 2). The Reynolds number is large for

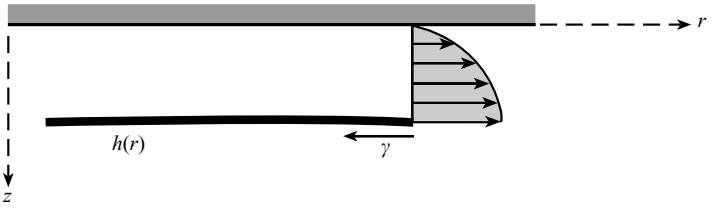

FIGURE 2. Schematic illustration of the velocity profile through the film in the fully developed region of flow, and opposing surface tension force. Velocity vectors are shown.

these flows, so a thin boundary layer will develop on the underside of the plate. Consequently, the thickness $h(r)$ and radial velocity $u(r, z)$ both vary spatially. The momentum flux may be found by integrating ρu^2 over the thickness of the film. The opposing surface tension force (per unit length) at the liquid–air interface has magnitude γ, since only one moving surface is present. Thus γ will replace 2γ in the analogy to (2.1). Since the velocity decreases with r due to viscous dissipation, there exists a radius R at which the momentum flux is no longer larger than the force due to surface tension, and the film can spread no further. This gives a location for the departure point. The equilibrium between the two forces resulting from these mechanisms leads to a condition analogous to that of Taylor:

$$\gamma = \int_0^{h(R)} \rho u^2(R, z)\, \mathrm{d}z. \tag{2.2}$$

We have considered only the steady state configuration, and not the initial wetting of the surface. It was observed experimentally that the liquid formed a local contact angle with the solid surface at the rim of the radial flow. This local contact angle was dependent on the wettability of the surface. Even so, the water bell departure radius was found to be independent of the surface, despite the formation of the local contact angle.

The water bell departure angle, formed between the solid surface and the falling film, was observed to have only a weak influence on the departure radius. Experiments showed that the departure radius remained constant to within 10 % throughout the range of possible departure angles.

While the complex flow in the vicinity of the departure point may influence the departure radius, it is experimentally found to be a secondary effect and is ignored to leading order. Its inclusion would require details of the corner flow, since this separates the fully developed flow along the plate from the local contact angle. This is not conducted here, for the above reasons.

We now have a means to find an expression for the departure radius R using the thickness and velocity profiles found for the radial flow by Watson (1964). Since the details of this solution are critical in the present context, a summary of the results of Watson (1964) and their application are presented.

2.1.1. *Laminar flow*

From the stagnation point at jet impingement, vorticity generated at the plate surface is swept radially downstream. Initially the boundary layer is thin, and the undisturbed potential flow continues near the free surface. Eventually, the viscous layer grows to contain the entire flow. To simplify matters, the flow is divided into three distinct regions. These are shown in figure 3 and defined as follows:

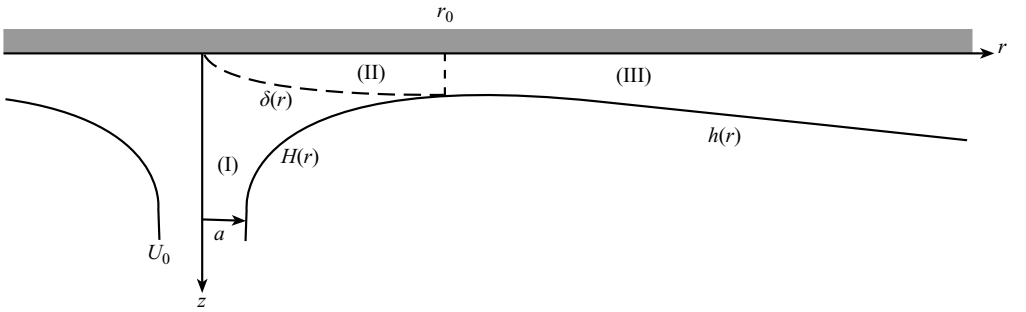

FIGURE 3. A schematic illustration of viscous flow regions in liquid flowing radially over the underside of a horizontal plate (Watson 1964). Gravity is assumed to act normal to the plate.

(I) The incoming potential flow, with jet velocity U_0, continuing near the free surface;

(II) The growing boundary layer, thickness $\delta(r)$, near the solid surface, from the stagnation point to where it engulfs the entire flow at radius r_0. The total thickness in region (II) is $H(r)$;

(III) The fully developed region, thickness $h(r)$, in which the boundary layer equations describe flow throughout the film.

Importantly, the transition between these regions is continuous. However, by solving the three problems separately and forming a composite solution, a good approximation to this complicated problem may be found. We also observe that the free surface of the jet prior to impingement on the top plate is parallel to the direction of flow, indicating approximately irrotational flow (see figure 1); the zero shear stress condition at the jet surface generates vorticity that diffuses into a thin layer near the free surface (Batchelor 1967).

To begin, we focus on the fully developed region (III). When viscous effects are present all the way to the free surface, the flow satisfies the boundary layer equations (see for example Landau & Lifshitz 1959):

$$\frac{\partial(ru)}{\partial r} + \frac{\partial(rw)}{\partial z} = 0, \tag{2.3}$$

$$u\frac{\partial u}{\partial r} + w\frac{\partial u}{\partial z} = \nu\frac{\partial^2 u}{\partial z^2} - g\frac{\mathrm{d}h}{\mathrm{d}r}. \tag{2.4}$$

Since the problem is axisymmetric, we use a cylindrical coordinate system (r, φ, z). Here u and w are, respectively, the r and z components of velocity, ν is the kinematic viscosity and g is gravitational acceleration. The influence of gravity is small since the thickness gradient in the radial direction of the thin film is negligible compared with the other length scales in the flow. To quantify the relative importance of the terms in the momentum equation, Clanet (2001) conducted an order of magnitude analysis on the gravitational pressure and viscous terms. Using results obtained in the inviscid limit, Clanet showed that the ratio of viscous to gravitational pressure terms $\approx 8\nu U_0 r^4/(ga^6)$, where a is the radius of the jet (see figure 3). In the current problem $\nu \sim 10^{-5}$ m^2 s^{-1}, $U_0 \sim 3$ m s^{-1} and $a \sim 5 \times 10^{-3}$ m, hence this dimensionless group exceeds 10 when $r > 2a$; note that this dimensionless group increases in proportion to r^4, and thus the effects of gravity diminish drastically along the plate. Consequently viscous stresses dominate gravitational pressure, so the gravitational body force term may be neglected in (2.4). Using this simplification, the present problem is equivalent

to that of Watson (1964), who considered a vertical jet falling on to a flat plate. Since the viscosity $\mu_{air} \ll \mu_{water}$, the shear stress at the free surface can be neglected. Equations (2.3) and (2.4) are then to be solved subject to

$$u(r, 0) = w(r, 0) = 0, \tag{2.5}$$

$$\left.\frac{\partial u}{\partial z}\right|_{z=h(r)} = 0, \tag{2.6}$$

$$Q = 2\pi r \int_0^{h(r)} u \, \mathrm{d}z, \tag{2.7}$$

where $h(r)$ is the film thickness and Q is the volumetric flow rate. In region (III), we search for a similarity solution of the form

$$u = U(r) f(\eta), \quad \text{where} \quad \eta = \frac{z}{h(r)}. \tag{2.8}$$

$U(r)$ is the free-surface velocity, and the boundary conditions are

$$f(0) = 0, \quad f(1) = 1, \quad f'(1) = 0. \tag{2.9}$$

Watson (1964) showed that the equation of motion (2.4) can be simplified with the conditions (2.9) to give the differential equation

$$(f')^2 = c^2(1 - f^3), \tag{2.10}$$

where

$$c = \int_0^1 (1 - x^3)^{1/2} dx = \frac{\sqrt{\pi}\,\Gamma\left(\frac{4}{3}\right)}{\Gamma\left(\frac{5}{6}\right)} \approx 1.402. \tag{2.11}$$

The constant volume flux condition (2.7) can then be written

$$rh(r)U(r) = \frac{3\sqrt{3}c^2 Q}{4\pi^2}. \tag{2.12}$$

Following this, the required solutions for the velocity and thickness profiles in the fully developed region of flow (III) are

$$U(r) = \frac{27c^2}{8\pi^4} \frac{Q^2}{\nu(r^3 + l^3)}, \tag{2.13}$$

$$h(r) = \frac{2\sqrt{3}\pi^2}{9} \frac{\nu(r^3 + l^3)}{Qr}, \tag{2.14}$$

where l is a length constant, to be determined by the matching of solutions between regions (I), (II) and (III) in figure 3. Watson gave a solution for f in terms of Jacobi elliptic functions. Here we present a simplification.

A power series approximation to the solution of (2.10) on $\eta \in [0, 1]$ is developed. We note that $f(0) = 0$, and so set

$$f(\eta) = a_1\eta + a_2\eta^2 + a_3\eta^3 + \cdots. \tag{2.15}$$

Substituting this into (2.10), and equating terms by order of η, we reach a series representation for f:

$$f(\eta) = c\eta - \frac{(c\eta)^4}{8} + \frac{(c\eta)^7}{112} - \frac{(c\eta)^{10}}{1792} + \frac{3(c\eta)^{13}}{93184} - \frac{37(c\eta)^{16}}{20873216} + O\left(\eta^{19}\right). \tag{2.16}$$

This gives a remarkably good approximation to the solution of (2.10) for $\eta \in [0, 1]$, the maximum absolute error being 0.005 %.

In region (II), the flow satisfies a similarity solution

$$u = U_0 f(\eta'), \quad \text{where} \quad \eta' = \frac{z}{\delta(r)}, \tag{2.17}$$

and the thickness of the growing boundary layer is

$$\delta(r) = \left(\frac{\sqrt{3}\pi c^3}{\pi - c\sqrt{3}} \frac{a^2 \nu r}{Q} \right)^{1/2} \approx 4.585 \left(\frac{a^2 \nu r}{Q} \right)^{1/2}. \tag{2.18}$$

The total thickness in regions (I) and (II) is

$$H(r) = \frac{a^2}{2r} + \delta(r) \left(1 - \frac{2\sqrt{3}\pi}{9c^2} \right). \tag{2.19}$$

Finally, Watson showed that the boundary layer first contains the entire flow at

$$r_0 = \left(\frac{9\sqrt{3}c(\pi - c\sqrt{3})}{16\pi^3} \frac{a^2 Q}{\nu} \right)^{1/3} \approx 0.3156 \left(\frac{a^2 Q}{\nu} \right)^{1/3}, \tag{2.20}$$

and that

$$l = \left(\frac{9\sqrt{3}c(3\sqrt{3}c - \pi)}{16\pi^3} \frac{a^2 Q}{\nu} \right)^{1/3} \approx 1.798\ r_0. \tag{2.21}$$

For the dimensions of our problem, r_0 is typically much less than the radius at which the film leaves the solid surface, and hence viscous effects are important in nearly the entire flow. This concludes the findings of Watson (1964) for laminar flow.

For $r < r_0$ the boundary layer thickness is given by (1.18), and the total film thickness by (2.19). For $r > r_0$, this thickness varies according to (2.14). The velocity in the inviscid region ($r < r_0$, $z > \delta(r)$) is U_0, and in the boundary layer is given by $u = U(r) f(\eta)$. Here $U(r) = U_0$ for $r < r_0$, and is otherwise defined in (2.13). Recall that f is given by (2.16), and finally the transition point r_0 by (2.20).

Critical radius (laminar flow)

These results are now used to solve (2.2). Since $R \gg r_0$ in practice, the departure radius occurs in the fully developed region (III). This leads to

$$\gamma = \int_0^{h(R)} \rho U^2(R) f^2(\eta) \mathrm{d}z = \rho U^2(R) h(R) \int_0^1 f^2(\eta) \mathrm{d}\eta. \tag{2.22}$$

Using the differential equation (2.10), the integral may be evaluated as

$$\int_0^1 f^2(\eta) \mathrm{d}\eta = \frac{1}{c} \int_0^1 \frac{f^2}{\sqrt{1 - f^3}} \mathrm{d}f = \frac{2}{3c}. \tag{2.23}$$

Substituting (2.23) into (2.22) then yields the required condition for the departure radius:

$$R\left(R^3 + l^3\right) = \frac{27\sqrt{3}c^3 \rho Q^3}{16\pi^6 \nu \gamma} \equiv \lambda. \tag{2.24}$$

While an analytic solution exists for (2.24), it is complicated in nature, and gives little information on the importance of the many parameters. For this reason, we consider

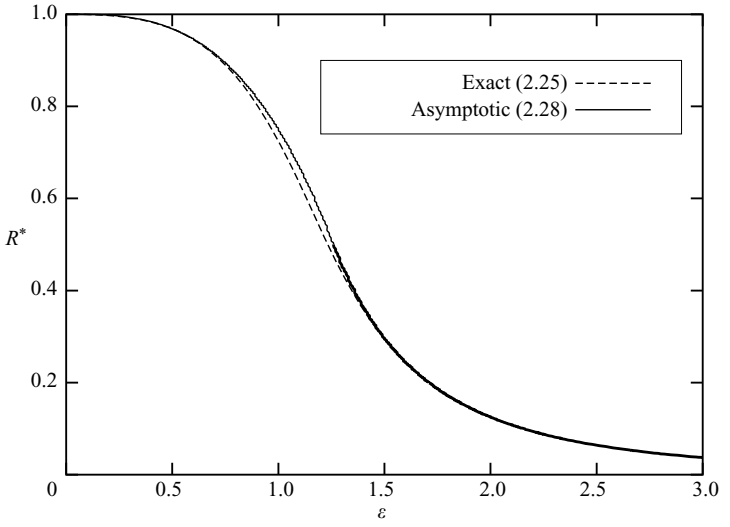

FIGURE 4. Comparison of asymptotic and exact solutions to (2.25).

two asymptotic limits. With R^* defined by $R = \lambda^{1/4} R^*$, (2.24) becomes

$$R^* \left(R^{*3} + \varepsilon^3 \right) = 1, \quad \text{where} \quad \varepsilon = \frac{l}{\lambda^{1/4}}. \tag{2.25}$$

This equation now contains only one parameter, and we solve this for the limiting cases of small and large ε. Equation (2.25) has only one real, positive root. For small ε, we expand the analytic solution to (2.25) as a power series in ε:

$$R^* = 1 - \frac{1}{4}\varepsilon^3 - \frac{1}{32}\varepsilon^6 + O\left(\varepsilon^{12}\right). \tag{2.26}$$

For $\varepsilon \gg 1$, we expand the same solution as a power series in ε^{-1}:

$$R^* = \varepsilon^{-3} - \varepsilon^{-15} + O\left(\varepsilon^{-27}\right). \tag{2.27}$$

Since both expansion parameters are small, we make an approximation by truncating the two series to order 3. Note the two solutions for R^* intersect when $\varepsilon = 2^{1/3}$. Thus we form the (approximate) composite solution

$$R^* \approx \begin{cases} 1 - \dfrac{1}{4}\varepsilon^3 & \varepsilon < 2^{1/3}, \\ \varepsilon^{-3} & \varepsilon \geqslant 2^{1/3}. \end{cases} \tag{2.28}$$

Further analysis shows the error in choosing the composite solution is no more than 6.8 % for all values of ε (see figure 4). The error attains a maximum for $\varepsilon \sim 2^{1/3}$, and is otherwise negligible. This accuracy is sufficient for the current purpose. Importantly, the above solution is valid in region (III) only, i.e. $R > r_0$. From (2.24), this corresponds to $\varepsilon \leqslant 1.113$, and the first solution is chosen; this parameter range is typical for our problem. Thus, we obtain the following result for the water bell departure radius:

$$R = \lambda^{1/4} \left(1 - \frac{1}{4} \left(\frac{l}{\lambda^{1/4}} \right)^3 + O\left(\left(\frac{l}{\lambda^{1/4}} \right)^6 \right) \right). \tag{2.29}$$

Since $l/R \ll 1$ for the flows we consider, we neglect l^3 in (2.29), which then leads to an excellent approximation for the departure radius. We thus observe the zeroth order term, denoted R_0, is given by

$$R_0 = \left(\frac{81c^3}{16\sqrt{3}\pi^6}\frac{\rho Q^3}{\nu\gamma}\right)^{1/4} \approx 0.3025\left(\frac{\rho Q^3}{\nu\gamma}\right)^{1/4}. \tag{2.30}$$

This result predicts that the departure radius $R \propto Q^{3/4}$, to leading order.

It is interesting to note that if we define $\hat{R} = R/a$, where a is the jet radius, the asymptotic limits for the departure radius may be expressed in dimensionless form:

$$\left.\begin{aligned} \hat{R} &\sim 0.0507\, We, & R \ll l,\\ \hat{R} &\sim 0.3025\,(Re\,We)^{1/4}, & R \gg l, \end{aligned}\right\} \tag{2.31}$$

where the Reynolds and Weber numbers are given respectively by

$$Re = \frac{Q}{a\nu}, \quad We = \frac{\rho Q^2}{a^3\gamma}. \tag{2.32}$$

We emphasize that the $R \ll l$ result is not obtained from (2.30), but from a re-analysis using the inviscid flow in region (I), and shows the departure radius results from the competition between inertia and surface tension; this is not the case typically encountered, as mentioned above. When $R \gg l$, the boundary layer contains the entire film thickness and the departure radius is determined from competition between inertia and the combined effects of viscosity and surface tension. Importantly, it is the latter case that applies to the water bells described in Part 1.

2.1.2. *Turbulent flow*

We now investigate the case of turbulent flow. Using the stability analysis of Lin (1945), Watson (1964) found that the flow along the plate will be laminar provided the local Reynolds number $Re_1 = U\delta_1/\nu < 275$, where δ_1 is the displacement thickness of the boundary layer. This Reynolds number attains a maximum at $r = r_0$, which is the point where the boundary layer first comprises the entire flow. Requiring $Re_1 < 275$ at $r = r_0$ is equivalent to the condition $Re = Q/(a\nu) < Re_c = 2.57 \times 10^4$, since the nozzle radius a can be directly related to the film thickness at $r = r_0$.

For flows exceeding this critical Reynolds number, Watson examined the situation in which the flow is turbulent along the entire plate. Following Glauert (1956), an eddy viscosity is introduced, and a similarity solution for the velocity distribution is constructed. This analysis proceeds in a similar fashion as that for laminar flow. As before, the growing boundary layer contains the whole flow for $r > r_0$, where

$$r_0 = \frac{\left[80\left(A - \frac{2}{9}\right)\right]^{4/9}}{(224\pi A^5)^{1/9}}\left(\frac{a^8 Q}{\nu}\right)^{1/9} \approx 1.218\left(\frac{a^8 Q}{\nu}\right)^{1/9}, \tag{2.33}$$

where $A = \sqrt{\pi}\Gamma(8/9)/(9\Gamma(25/18)) \approx 0.239$. Values of r_0 from (2.33) are typically much less than that of the water bell departure radius, so again, only the fully developed region of flow is relevant for solving (2.2). The important results of Watson (1964) for this region are as follows. A similarity solution for the velocity is constructed: $u = U(r)F(\eta)$, $\eta = z/h(r)$, where the free-surface velocity and film

thickness profiles are given by

$$U(r) = \left(\frac{100}{9(14\pi^5 A^5)^{1/4}}\right)\frac{Q^{5/4}}{\nu^{1/4}(r^{9/4}+l^{9/4})}, \tag{2.34}$$

$$h(r) = \left(\frac{9k(14\pi A)^{1/4}}{200}\right)\frac{\nu^{1/4}(r^{9/4}+l^{9/4})}{Q^{1/4}r}, \tag{2.35}$$

respectively, where $k = \sqrt{\pi}\Gamma(7/9)/(9\Gamma(23/18)) \approx 0.260$,

$$l = \frac{[20(1-2A)]^{4/9}}{(14\pi A^5)^{1/9}}\left(\frac{a^8 Q}{\nu}\right)^{1/9} \approx 4.126\left(\frac{a^8 Q}{\nu}\right)^{1/9} \tag{2.36}$$

and F satisfies $(F^6F')^2 = k^2(1-F^9)$. This concludes the analysis of Watson (1964) for turbulent flow.

Critical radius (turbulent flow)

Using these results, the criterion for maximum radial extension (2.2) becomes

$$\gamma = \rho U^2(R)h(R)\int_0^1 F^2(\eta)\mathrm{d}\eta = \frac{2\rho}{9k}U^2(R)h(R). \tag{2.37}$$

This leads to the condition for the radius of departure from the solid surface for the case of turbulent flow,

$$R(R^{9/4}+l^{9/4}) = \frac{100\,\rho Q^{9/4}}{81(14\pi^9 A^9)^{1/4}\,\gamma\nu^{1/4}} \equiv \lambda_2. \tag{2.38}$$

Here an analytic solution is not possible. As for the laminar case, a leading order solution is presented,

$$R_0 = \left(\frac{10^8}{3^{16}(14\pi^9 A^9)}\frac{\rho^4 Q^9}{\gamma^4\nu}\right)^{1/13} \approx 1.062\left(\frac{\rho^4 Q^9}{\gamma^4\nu}\right)^{1/13}. \tag{2.39}$$

This approximation is valid when $l \ll R$, which we expect since $O(l) \sim O(r_0)$, c.f. (2.33) and (2.36). The error in taking this leading order term instead of the numerical solution to (2.38) is less than 10 % provided $l/R < 0.67$; a condition that is satisfied in practice. This result indicates that for turbulent flow the leading order dependence of water bell departure radius on flow rate is $R \propto Q^{9/13} \sim Q^{0.69}$. Interestingly, the dependence on flow rate is slightly weaker for the case of turbulent flow in comparison with laminar flow, which yielded $R \propto Q^{0.75}$.

In dimensionless form, the asymptotic limits for the departure radius in the case of turbulent flow become

$$\left.\begin{aligned} \hat{R} &\sim 0.0507\,We, && R \ll l,\\ \hat{R} &\sim 1.0621\,(Re\,We^4)^{1/13}, && R \gg l, \end{aligned}\right\} \tag{2.40}$$

where the Reynolds and Weber numbers are given by (2.32). Note that the inviscid solution for $R \ll r_0$, i.e. region (I), is identical to (2.31), as expected and required. Interestingly, (2.40) shows that the dominant physical mechanisms for $R \gg l$, i.e. region (III), are also similar to the case of laminar flow, (2.31), albeit to a different degree.

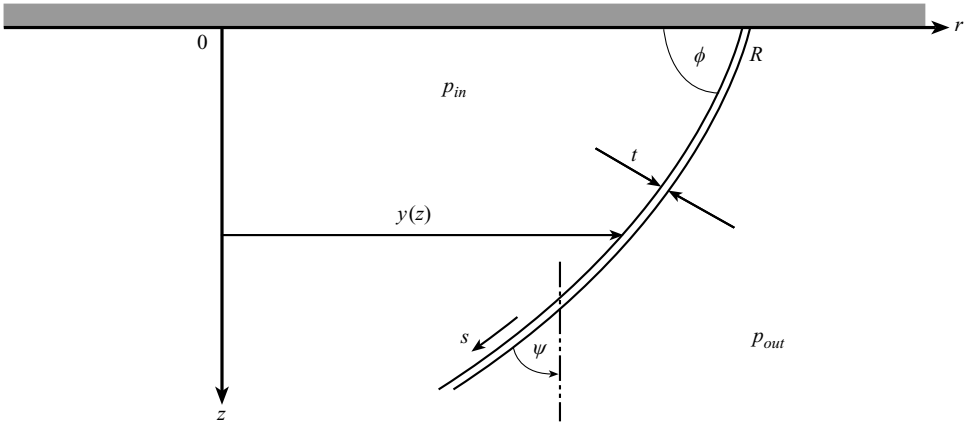

FIGURE 5. Schematic of water bell surface.

2.2. *Bell shape*

We now investigate the shape of the liquid curtain using standard inviscid water bell theory (Boussinesq 1869*b*).

The theory is derived with reference to figure 5, and consists of a force balance normal to the stream. By considering the forces resulting from (i) gravity, (ii) pressure difference across the surface of the bell and (iii) surface tension, Boussinesq derived the equation

$$2\gamma\left(\frac{\cos\psi}{y}-\frac{\mathrm{d}\psi}{\mathrm{d}s}\right)+\rho g t\sin\psi-\Delta p+\rho t u^2\frac{\mathrm{d}\psi}{\mathrm{d}s}=0, \tag{2.41}$$

where γ is the surface tension, ρ the density, g the gravitational acceleration, u the fluid velocity and $\Delta p = p_{in} - p_{out}$ is the pressure difference across the thin film. The latter is assumed to be constant and uniform. For effects of internal air circulation, see Parlange (1967). Here $y(z)$ is the distance from the bell surface to the z-axis, and ψ, s and t are defined in figure 5. The water bell angle of departure is denoted ϕ. For constant flow rate Q, continuity requires

$$Q = 2\pi y t u, \tag{2.42}$$

for all z. Using the dimensionless variables

$$\tilde{z}=\frac{z}{L},\quad \tilde{s}=\frac{s}{L},\quad Y=\frac{y}{L},\quad \tilde{u}=\frac{u}{u_0},\quad \text{where}\quad L=\frac{\rho Q u_0}{4\pi\gamma}, \tag{2.43}$$

and u_0 is the fluid velocity at the point of departure from the plate, Taylor (1959*a*) showed that (2.41) becomes

$$\frac{\cos\psi}{Y}-\frac{\mathrm{d}\psi}{\mathrm{d}\tilde{s}}-\alpha+\beta\frac{\sin\psi}{\tilde{u}Y}+\frac{\tilde{u}}{Y}\frac{\mathrm{d}\psi}{\mathrm{d}\tilde{s}}=0, \tag{2.44}$$

$$\alpha=\frac{\rho Q u_0\Delta p}{8\pi\gamma^2}, \tag{2.45}$$

$$\beta=\frac{\rho g Q}{4\pi\gamma u_0}. \tag{2.46}$$

The relevant length scale for the flow, L, is inversely proportional to the surface tension, hence larger surface tension will result in larger curvature in the water bell

shape. Notice that (2.44), and hence the path taken by the falling film, depends only upon two dimensionless parameters, α and β. The pressure difference Δp enters the governing equation only through α, while the β term accounts for gravity. Equation (2.44) can be further simplified by noting $Y'(\tilde{z}) = \tan\psi$, which leads to

$$Y''(\tilde{u} - Y) + \left(1 + \left(Y'\right)^2\right)\left(1 + \frac{\beta}{\tilde{u}}Y'\right) - \alpha Y\left(1 + \left(Y'\right)^2\right)^{3/2} = 0. \tag{2.47}$$

This is to be solved with the initial conditions

$$Y(0) = R/L, \tag{2.48}$$

$$Y'(0) = 1/\tan\phi, \tag{2.49}$$

where ϕ is the angle of departure from the plate, and R is the departure radius.

Note that the surface of the liquid film is itself a streamline, as well as a surface of constant pressure. The Bernoulli equation $u^2 = u_0^2 + 2gz$ in dimensionless form is

$$\tilde{u}^2 = 1 + 2\beta\tilde{z}, \tag{2.50}$$

where β is given by (2.46). This relation, together with (2.47)–(2.49) provides the governing equations for the falling sheet. We now consider the relative importance of gravity and pressure. Using typical dimensions of the bell, the Froude number $u_0/(gR)^{1/2}$ is $O(1)$. Thus the gravitational and inertial forces are comparable, and hence the β term must be retained. Experiments show the bell can be made to form a perfect cylindrical shape. In this case, all derivatives of Y with respect to $\tilde{z}$ vanish, and (2.47) reduces to $\alpha Y = 1$. Clearly, in this case α is non-zero. Thus the analytic solution presented by Taylor (1959*a*) to (2.47)–(2.50), for the case $\alpha = \beta = 0$ is not applicable. Instead, we consider a leading order asymptotic theory, and the numerical solution.

2.2.1. *Strong gravity approximation*

Recall the force balance equation (2.41). Using the geometric relation $y'(z) = \tan\psi$, this can be written as

$$-\frac{2\gamma\, y''}{\left(1 + (y')^2\right)^{3/2}} + \frac{2\gamma}{y\sqrt{1 + (y')^2}} + \frac{\rho g t\, y'}{\sqrt{1 + (y')^2}} - \Delta p = -\frac{\rho t u^2 y''}{\left(1 + (y')^2\right)^{3/2}}. \tag{2.51}$$

An appropriate scale for y is $y \sim R$, where R is the radius of departure from the plate. The thin fluid film attached to the horizontal plate near radius R acts as a reservoir for the falling film. We consider a gravity dominated flow, i.e. gravitational forces are much larger than those due to surface tension. In this limiting case, we expect the fluid to 'fall' approximately vertically, and hence the length scale for z will be very large compared to R, the length scale for y. We therefore scale $z \sim \Lambda$, where $\Lambda \gg R$. Scaling (2.51) reveals

$$\frac{2\gamma\left(\frac{R}{\Lambda}\right)^2}{\left(1 + \left(\frac{R}{\Lambda}\right)^2\right)^{3/2}} + \frac{2\gamma}{\sqrt{1 + \left(\frac{R}{\Lambda}\right)^2}} + \frac{\rho g t R\left(\frac{R}{\Lambda}\right)}{\sqrt{1 + \left(\frac{R}{\Lambda}\right)^2}} + \Delta p R \sim \frac{\rho t u^2\left(\frac{R}{\Lambda}\right)^2}{\left(1 + \left(\frac{R}{\Lambda}\right)^2\right)^{3/2}}. \tag{2.52}$$

Importantly, $\Lambda \gg R$ implies $(R/\Lambda)^2 \ll 1$, and hence the first term on the left-hand side, and the term on the right may be neglected in this strong gravity limit. The

nonlinearities appearing in the denominators may also be removed for the same reason. Equation (2.52) then reduces to

$$\frac{2\gamma}{R} + \frac{\rho g t R}{\Lambda} + \Delta p \sim 0. \tag{2.53}$$

Balancing the first and second terms gives

$$\frac{2\gamma}{\rho g t R} \sim \frac{R}{\Lambda} \ll 1. \tag{2.54}$$

Thus the strong gravity limit formally corresponds to this inequality. Physically this means that the pressure difference across the film $2\gamma/R$ is much less than the gravity pressure difference $\rho g t$ due to the film thickness. We keep only the terms in (2.51) equivalent to those in (2.53). The equation is again scaled using the dimensionless variables (2.43), and an approximation to the governing equation is formed. In the strong gravity limit, Y' and Y'' being small, (2.47) reduces to

$$1 + \frac{\beta}{\tilde{u}} Y'(\tilde{z}) - \alpha Y(\tilde{z}) = 0. \tag{2.55}$$

Since the order has been reduced, we now need only one initial condition, the departure point R/L, which is specified by (2.29). As we shall see below, this is a valid simplification in this limit.

From the results of § 2.1, we determine the initial dimensions of the falling film. The velocity is considered constant across the thickness of the film, and the initial velocity is denoted u_0. Consider the bounding free streamline close to the departure point. The kinetic energy of a fluid particle at the surface must be conserved around the corner on this streamline, i.e.

$$u_0 = U(R), \tag{2.56}$$

where U and R are given by (2.13) and (2.29), respectively. We neglect the transition region of flow between the horizontal radial flow and the point in the descending film where uniform velocity is achieved across the film thickness t. Eliminating Q from (2.12) and (2.42) then gives the initial film thickness:

$$t(0) = \frac{2\pi}{3\sqrt{3}c^2} h(R). \tag{2.57}$$

The shape of the falling sheet may now be calculated. The solution to (2.55), in dimensional form, is

$$y(z) = \begin{cases} R + \dfrac{u_0^2}{3\beta g}\left[1 - \left(1 + \dfrac{2g}{u_0^2} z\right)^{3/2}\right], & \alpha = 0, \\ \dfrac{\beta u_0^2}{\alpha g} + \left(R - \dfrac{\beta u_0^2}{\alpha g}\right) \exp\left[-\dfrac{\alpha}{3\beta^2}\left(1 - \left(1 + \dfrac{2g}{u_0^2} z\right)^{3/2}\right)\right], & \alpha \neq 0. \end{cases} \tag{2.58}$$

This solution is formally valid in the asymptotic limit of strong gravity, as specified in (2.54). The $\alpha = 0$ case is appropriate when $\Delta p = 0$, i.e. the inside of the bell is vented to atmosphere.

2.2.2. *Numerical solution*

The 'exact' bell shape is obtained using the method of Brunet *et al.* (2004). This relies on a comparison between the fluid velocity and the 'sonic' velocity, defined

to be

$$u_s = \sqrt{\frac{2\gamma}{\rho t}}. \tag{2.59}$$

This is not only the velocity of antisymmetrical waves propagating on a fluid sheet (Taylor 1959*b*), but also that of the receding edge of a punctured sheet (Culick 1960).

For the bells in question, calculations show that when the fluid departs the plate, its velocity is 'subsonic'. Since the velocity increases as the fluid falls, a sonic point exists. In dimensionless variables, this point occurs when $Y = \tilde{u}$, and here (2.47) reduces to an algebraic condition for the derivative:

$$1 + \frac{\beta}{\tilde{u}} Y'^{*} - \alpha \tilde{u} \sqrt{1 + Y'^{*2}} = 0, \tag{2.60}$$

where Y^* denotes the value of the function, and Y'^* the gradient of the function at the sonic point. Since the initial departure point is known to be R/L, (2.47) may be solved by initially guessing $\tilde{z}^*$, the sonic point. $Y(\tilde{z}^*) = \tilde{u}$ is then immediately specified, and $Y'(\tilde{z}^*)$ can be calculated. Once these two quantities are known, the governing equation may be solved back to $z = 0$, and tested against the initial condition. An iterative shooting method then gives a full numerical solution to (2.47).

2.2.3. *Changing flow rate*

When the fluid leaves the plate for the first time, the film has not yet coalesced to form a bell. No air is cut off from the atmosphere until the sheet is complete, and so in this case there is no pressure difference across the surface of the bell. While we hold Q at the initial flow rate, $\Delta p = 0$, and hence $\alpha = 0$ for the constant flow rate problem.

The most interesting shapes are produced when, after the bell has been formed, the flow rate is altered (see Part 1). For an increased flow rate, the radius of departure R occurs further from the impact point of the jet and the film is observed experimentally to creep up the central pipe. While decreasing Q reduces R, the bottom of the bell expands radially. Here, we aim to predict the evolving bell shape, for varying flow rates, given an initial flow rate.

When the bell is initially formed, a fixed amount of gas is trapped by the flowing film. The mass of air inside the bell must therefore be conserved. We now estimate the pressure difference Δp across the film. Recall that the bell can be made to form a perfect cylinder with vertical sides. In this case, (2.47) reduces to $\alpha = L/R$, or

$$\Delta p = \frac{2\gamma}{R}, \tag{2.61}$$

which for these bells is of the order of 1 Pa. Clearly, the pressure change induced here is negligible compared to atmospheric pressure. Thus, to leading order, the gas can be considered incompressible and conservation of mass immediately implies conservation of volume.

As the flow rate changes, so too does R. For all flow rates, the correct bell shape must satisfy (2.55), (2.50), the initial condition $Y(0) = R/L$ and conserve its internal volume. The following method is used to determine the evolving bell shape. Note that in the following $y(z)$ may refer to either the strong gravity approximation (2.58), or to the numerical solution of (2.47).

Method of solution

(i) The bell is first formed: set $\Delta p = 0$, i.e. $\alpha = 0$, and solve for the initial shape $y(z)$.

(ii) Calculate the internal volume

$$V = \int_0^{z_c} \pi \left[y^2(z) - P^2(z) \right] \mathrm{d}z, \tag{2.62}$$

where $P(z)$ is the radial dimension of the pipe at height z, and z_c is defined to be (a) the point the film intersects the pipe, if it does, or (b) the total height of the bell if it does not intersect the pipe.

(iii) Alter the flow rate. This results in a new initial condition $Y(0) = R/L$, through the dependence of R on Q. We initially provide an estimate for $\alpha = \bar{\alpha}$. Let $Y_{\bar{\alpha}}(\tilde{z})$ be the result obtained by setting $\alpha = \bar{\alpha}$ in (2.47) and solving, and $y_{\bar{\alpha}}(z)$ its dimensional form.

(iv) Define the volume as a function of $\bar{\alpha}$:

$$V(\bar{\alpha}) = \int_0^{z_{c\bar{\alpha}}} \pi \left[y_{\bar{\alpha}}^2(z) - P^2(z) \right] \mathrm{d}z, \tag{2.63}$$

where $z_{c\bar{\alpha}}$ is defined in the same way as z_c.

(v) Numerically find $\bar{\alpha}$ such that $V(\bar{\alpha}) = V$.

(vi) The solution from step (v) is the required α for volume conservation. The correct bell shape is then given by $y_\alpha(z)$. Once α has been determined, (2.45) may be rearranged allowing the resultant pressure difference to be calculated.

If the conditions at which a bell is originally formed are known, this algorithm allows us to determine the bell shape as it changes with flow rate.

3. Comparison with experimental results

The theoretical predictions of § 2 are now compared with experimental results. Departure radius and bell shape were measured for a variety of flow rates and conditions, using three different fluids – two glycerol–water mixtures (70–30 and 90–10 w/w) and a Triton X-100 solution. Details of the experiments are presented in the companion paper (Part 1).

3.1. *Departure radius*

For each of the liquids, measurements of the radius at which the liquid departed the plate were taken at a range of flow rates. These results are discussed below.

The Reynolds number $Re = Q/(a\nu)$ was calculated for each of the three liquids. It was found that $10^2 < Re < 10^3$ for the 90–10 (w/w) glycerol–water mixture, $10^3 < Re < 10^4$ for the 70–30 (w/w) glycerol–water mixture and $10^4 < Re < 10^5$ for the Triton X-100 solution. As stated in § 2.1.2, it is expected that the flow should be laminar provided $Re < Re_c = 2.57 \times 10^4$. Under this criterion, both glycerol–water flows will be laminar throughout, while the experiments using surfactant solution took place in the transition regime between laminar and turbulent flow.

Figure 6 shows the laminar theory compared with experimental measurements of the departure radius R for each of the three fluids. The experimental data have been scaled and compared with the leading order laminar flow theory, (2.30). As can be seen, (2.30) captures the experimental behaviour very well, even though the viscosity was varied by two orders of magnitude. In all cases, the radius of the impinging jet was 4 mm. This theory contains no fitting parameters. It is significant that the

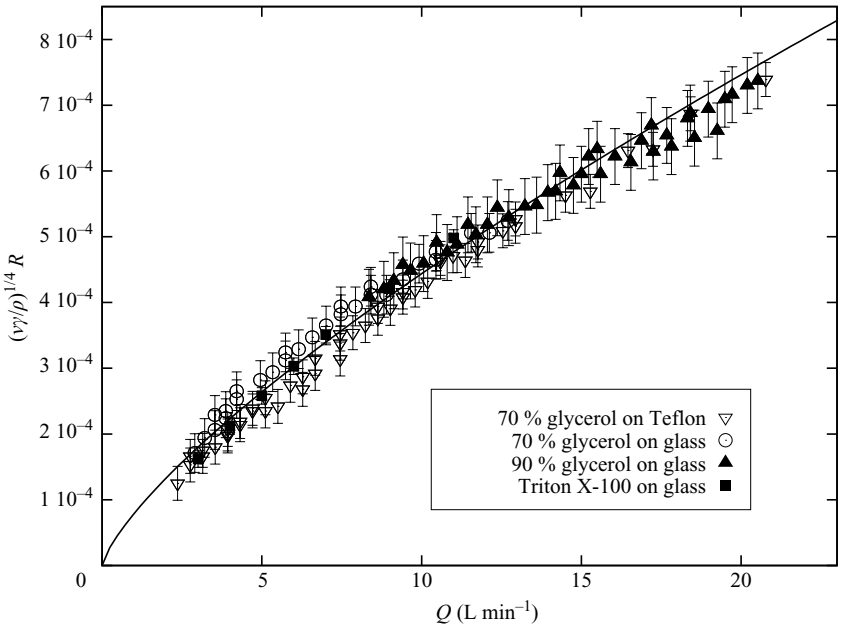

FIGURE 6. Departure radius as a function of flow rate: comparison of (2.30) (leading order theory) with experimental results. Liquid properties are presented in table 1 of Part 1.

relationship between departure radius and flow rate, $R \propto Q^{3/4}$, is accurately captured. In Part 1, a dimensional analysis of the experimental data was performed, suggesting the empirical relation

$$R = 0.31 \left(\frac{\rho^{0.26} Q^{0.74}}{\gamma^{0.26} \nu^{0.23}} \right). \tag{3.1}$$

This is remarkably close to the rigorous theoretical result given by (2.30), and provides further support for its validity. The leading order expression for the critical radius is independent of the diameter of the impinging jet, in agreement with experimental results (Part 1, Jameson *et al.* 2010).

Figure 7(*a*) gives a comparison between both the laminar and turbulent theories and experimental data for the Triton X-100 solution. In this case, the Reynolds number suggests the flow may be turbulent. The turbulent approximation given by (2.39), the numerical solution to (2.38) and the laminar result equation (2.30), give similar agreement with experimental measurements, although the laminar solution appears to be slightly closer to the data; possibly due to the turbulent motion not being fully developed. The close agreement between laminar and turbulent theories is fortuitous, and perhaps due to the measurements lying within the transition regime between laminar and turbulent flow. Rippling of the film surface was observed experimentally in some cases, suggesting the presence of turbulence.

It was not possible to form water bells using pure water, so a surfactant solution was used in order to obtain quantitative results for departure radius using a fluid of relatively low viscosity. The use of surfactant raises many issues. The no shear-stress condition at the free surface may not hold, due to non-uniform surfactant concentration and the resulting Marangoni stresses. Most experimental results were obtained using glycerol–water mixtures to eliminate these possible undesirable effects.

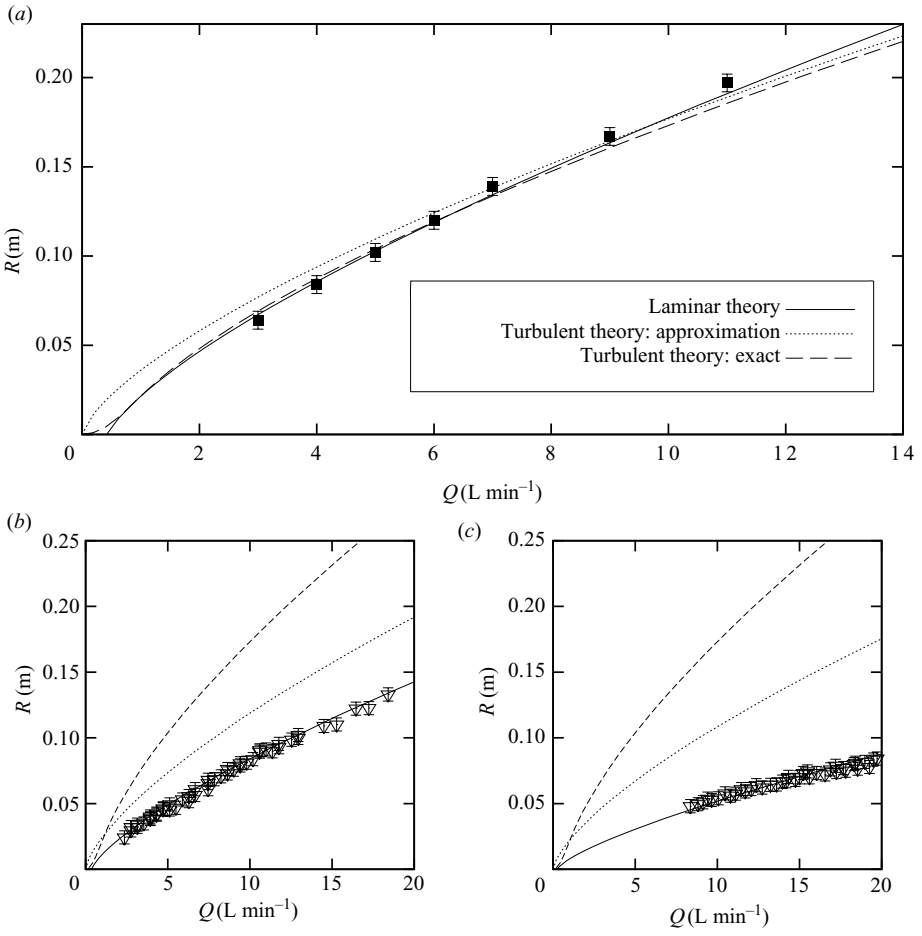

FIGURE 7. Departure radius as a function of flow rate: comparison of theory for laminar and turbulent flow with experimental results. (*a*) Triton X-100 solution water bells in the transition regime, (*b*) 70 % glycerol mixture and (*c*) 90 % glycerol mixture water bells in the laminar regime.

Importantly, such agreement between laminar and turbulent solutions was absent for the glycerol–water mixtures (for which $Re \ll Re_c = 2.57 \times 10^4$), which were well described by the laminar theory only. For completeness, the turbulent theoretical predictions are shown with the experiments and laminar result in figure 7(*b, c*).

All experimental data described above were obtained for water bells formed at the initial flow rate. No pressure difference existed across the surface of the bell, and no hysteresis was observed.

3.2. *Bell shape*

In this section, we distinguish between water bells formed at the initial flow rate, and bells at other flow rates where air is trapped. In the first case, no pressure difference exists between the inside and outside of bell. In the latter case, hysteretic effects were present.

In the first case, water bells were formed using a 70 % glycerol mixture. The surface of the water bell was broken using a tube in order to eliminate any possible pressure difference across the film. Photographs of the water bells were analysed to determine

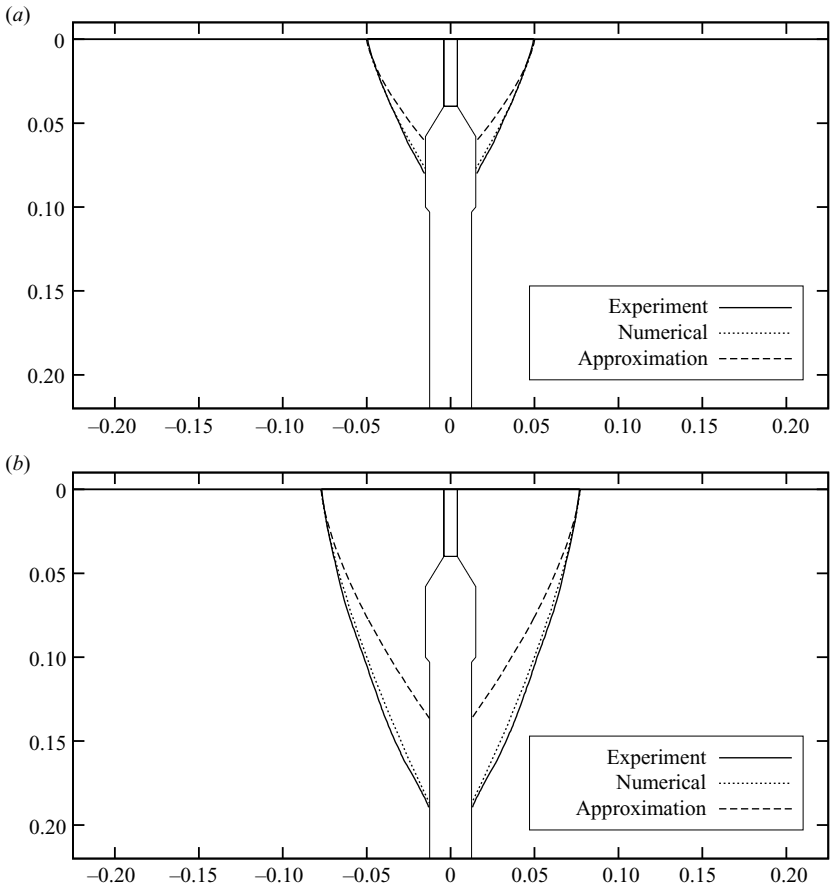

FIGURE 8. Predicted water bell shapes compared to experimental shapes. Water bells formed using a 70 % glycerol mixture, 4 mm jet radius and Teflon surface at a flow rate of (*a*) 6.0, (*b*) 10.5 L min^{-1}.

the bell shape. The height of the water bell was divided into 0.2 mm increments, and the radial dimension of the bell was measured at each point. Figure 8 shows the extracted shapes compared with both the strong gravity approximation, (2.58) and the numerical solution to (2.47). The exact solution quantitatively captures the bell shape very well, with the approximation being less accurate while capturing the dominant qualitative features.

A series of water bells displaying hysteretic effects were analysed for comparison with the theory.

Case 1: A 70 % glycerol mixture was used to form a water bell at a flow rate of 8.9 L min^{-1}. The flow rate was then increased to 13.7 L min^{-1}. The film remained closed throughout the experiment, trapping a fixed amount of air inside the bell. The departure radius increased and the bottom of the water bell was observed to creep up the central pipe as the flow rate increased, and volume appeared to be conserved. The departure angle ϕ at which the fluid departed the plate became smaller as the flow rate was increased. Eventually the pulled up film became unstable and broke. It is not known what determines the point of instability. Figure 9 allows visual comparison

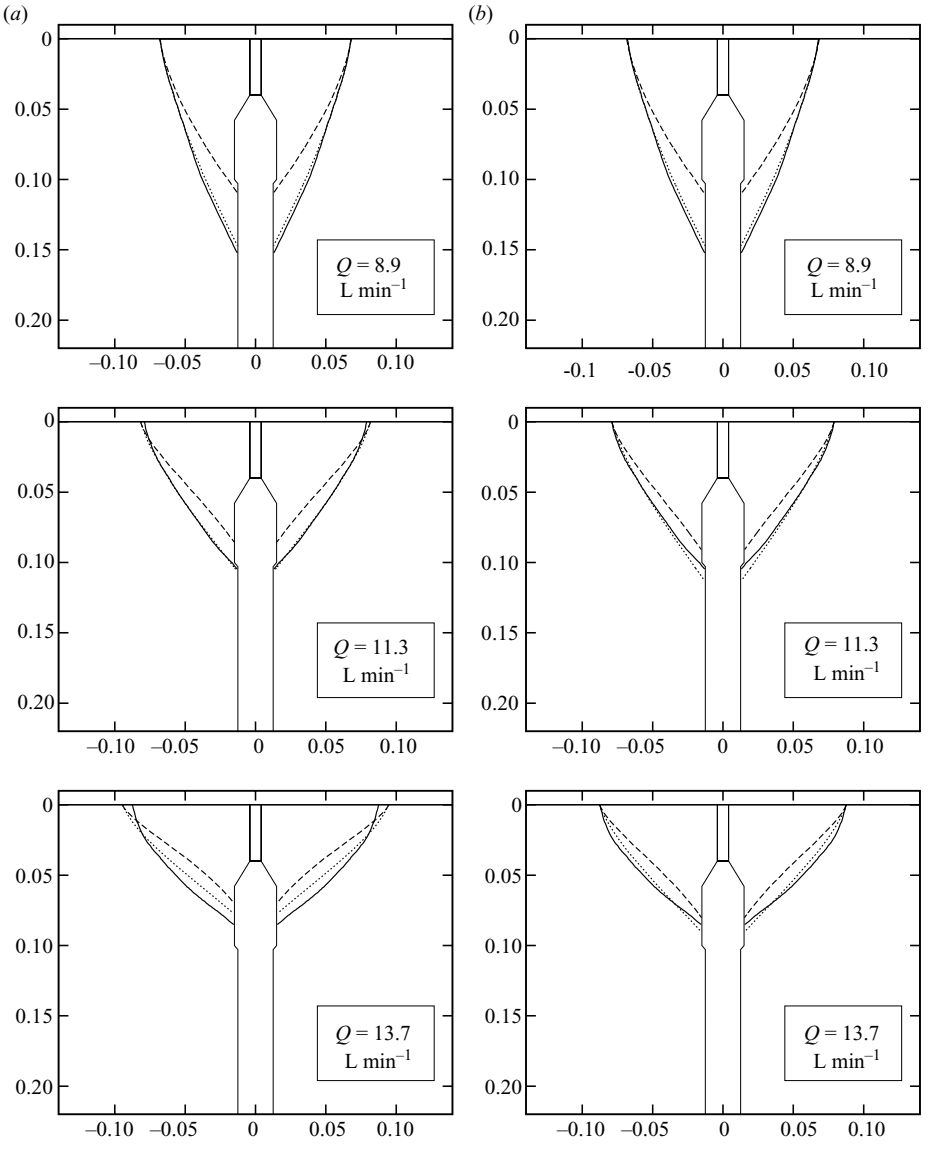

FIGURE 9. Predicted water bell shapes displaying hysteresis: increasing flow rate. Water bells formed using a 70 % glycerol mixture, 4 mm jet radius and Teflon surface. Shape extracted from experiment – solid line, numerical solution to (2.47) – dotted line, strong gravity approximation (2.58) – dashed line. (*a*) Full self-consistent model. (*b*) Experimental values for departure radius used as initial conditions.

of theory to experimental shapes. The shapes were calculated using the method of solution described in § 2.2.3.

It was observed that the departure radius was slightly dependent on the hysteresis of the flow. This meant that while the model is able to accurately predict the departure radius for the initial water bell in the sequence, there may be inaccuracy of up to 10 % as the flow rate is altered from its initial value. Since the protocol for determining water bell shape relies on volume conservation, an error in the departure radius will affect the entire bell shape. Thus we present two sets of results: (i) the shapes in

figure 9(*a*) are produced using the full self-consistent model, (ii) those in figure 9(*b*) are obtained by using the experimental value for the departure radius for each bell.

Note the good agreement between the exact numerical solution and experiment in all cases. We emphasize, the theory contains no fitting parameters, and only the flow rate was changed between figures. At flow rates away from that of initial formation, the theory is better able to predict the shape if the experimental value is used for departure radius. As yet no theory exists for the effect of hysteresis on departure radius, so we present this method as an alternative to the full model, which becomes more inaccurate as the flow rate is modified. Even so, we note that the quantitative difference between these two models is small.

The strong gravity approximation (2.58) is able to capture the qualitative features and dominant behaviour of the water bells under changing flow rate. The inaccuracy in the shapes is compounded by inaccuracy in the original volume, which then propagates through subsequent calculations.

Equation (2.45) indicates that the pressure inside the bell was 5.4 Pa less than the pressure outside the bell when the flow rate was 13.7 L min^{-1} using the numerical solution, and 9.4 Pa less using the strong gravity approximation. These pressure differences are negligible compared to atmospheric pressure, and so the condition of volume conservation remains valid even for these strongly hysteretic water bells.

Case 2: A 70 % glycerol mixture was used to form another water bell at a flow rate of 8.9 L min^{-1}. The flow rate was then decreased to 7.0 L min^{-1}. Again the film remained closed throughout the experiment, trapping a fixed amount of air inside the bell. The departure radius decreased and the bottom of the water bell was observed to creep down the central pipe as the flow rate increased, and volume appeared to be conserved. The departure angle ϕ became larger, approaching 90°, as the flow rate was decreased. These experimental shapes are shown in figure 10. The agreement with theoretical shapes is similar to the case of increasing flow rate. Here, the internal pressure was calculated to be 1.8 Pa (approximation) and 1.6 Pa (numerical) higher than the ambient.

The numerical method described above relies on the existence of a 'sonic' point. Experimentally this can be observed as the location at which a wake ceases to form behind an obstruction in the falling fluid film. In these experiments it was not possible to determine the location of the sonic point, since the wake disappeared at a point very close to the solid surface, possibly having interference from the radial flow on the underside of the plate. This means the entire water bell is supersonic apart from a small region near the solid surface. When calculating the shapes described above, it is necessary to determine the location of the sonic point. For all the shapes shown in figures 9 and 10, the sonic point was calculated to be between 2.5 and 3.8 mm beneath the solid surface, compared to a film length of 100–200 mm. These calculations are therefore consistent with the experimental observations.

3.3. *Water bell departure angle*

Once the bell shape has been calculated, the water bell departure angle may be determined using (2.49). In the case of the strong gravity approximation, this reduces to

$$\phi = \arctan\left(\frac{\alpha R - 1}{\beta}\right). \tag{3.2}$$

It was experimentally difficult to measure the water bell departure angle, due to the existence of a local contact angle at the solid surface. For this reason, tangents were drawn to the bell surface 1 cm below the horizontal plate, allowing this (macroscopic)

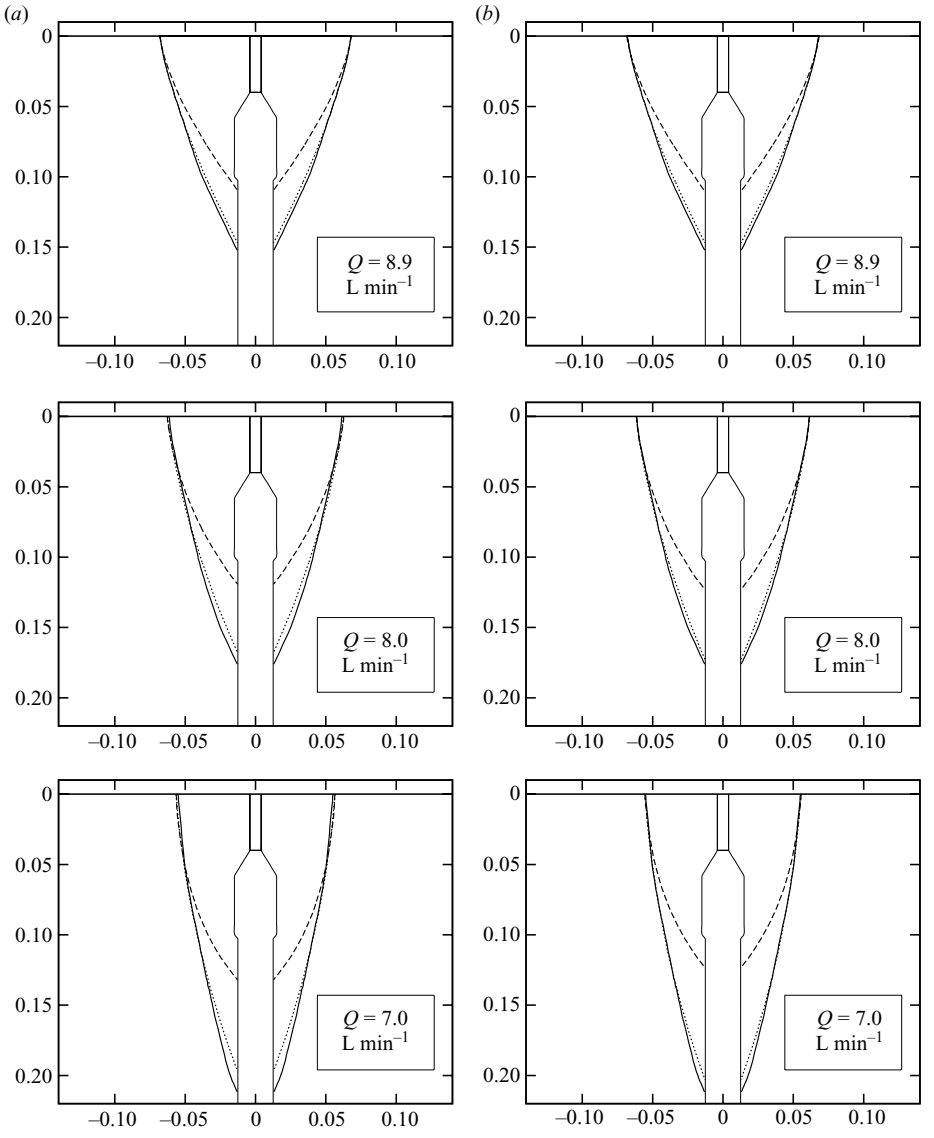

FIGURE 10. Predicted water bell shapes displaying hysteresis: decreasing flow rate. Water bells formed using a 70 % glycerol mixture, 4 mm jet radius and Teflon surface. Shape extracted from experiment – solid line, numerical solution to (2.47) – dotted line, strong gravity approximation (2.58) – dashed line. (*a*) Full self-consistent model. (*b*) Experimental values for departure radius used as initial conditions.

water bell departure angle to be determined. In this comparison with experiments, two calculations are shown for completeness. The theoretical departure angle calculated at $z = 0$ is presented along with the angle obtained using the gradient at $z = 0.01$ m to be consistent with the way in which experimental data points were obtained. Both these curves are presented in figure 11. Pressure difference across the surface of the bell was eliminated before each measurement, to remove effects of hysteresis. The models appear to capture the behaviour of the departure radius as a function of flow rate. The full numerical solution does lie closer to the experimental results, but is not

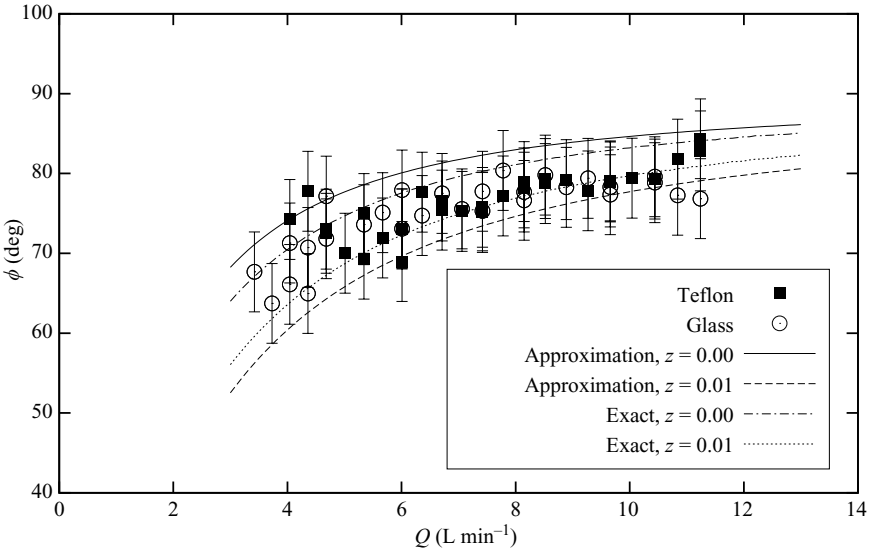

FIGURE 11. Departure angle as a function of flow rate: 70 % glycerol mixture, 4 mm jet radius.

appreciably more accurate. We also note that the nature of the surface (hydrophobic, hydrophilic) does not have a visible effect on the water bell departure angle.

4. Conclusions

We have developed a theoretical model to explain the water bells formed on the underside of an essentially infinite horizontal plate (Part 1, Jameson *et al.* 2010). These water bells are produced when an upward flowing liquid jet impinges normally on a horizontal plate from below, then spreads radially to an unspecified abrupt point and falls. These water bells exhibit a sharp departure from the solid surface. Large hysteretic effects are also displayed by the surface of the water bell upon change in flow rate, and are far more pronounced than in any type of water bell reported previously.

Experiments showed the departure radius is insensitive to the shape of the water bell. This observation was combined with the analytical work of Watson (1964) to calculate the radius at which the liquid leaves the horizontal plate. The leading order expression for the radius in the case of laminar flow is

$$R_0 = \left[\frac{81c^3}{16\sqrt{3}\pi^6}\frac{\rho Q^3}{\nu\gamma}\right]^{1/4} \approx 0.3025\left(\frac{\rho Q^3}{\nu\gamma}\right)^{1/4}.$$

This equation agrees well with experimental data spanning two orders of magnitude in fluid viscosity. An analogous equation for the case of turbulent flow is also presented, and agrees with measurements for flows at or near the turbulent regime.

Once the flow had departed the solid surface, the shape of the resulting thin film flow was calculated using conventional water bell theory, and subsequently married to the theory for flow in the thin film attached to the plate. The equations were solved (i) asymptotically in the strong gravity limit and (ii) numerically. The theory contains no fitting parameters, and for closed water bells which trap a fixed amount of air, captures the shape and all dominant features of the phenomenon. For open bells

whose inside is vented to the atmosphere, and therefore volume (mass) conservation is no longer satisfied, the shapes are also correctly predicted.

Taken as a whole, the theory yields quantitative results that compare favourably with experiments over a wide parameter range, and describes the dominant physical processes at work in the formation of the novel water bells reported in Part 1 (Jameson *et al.* 2010).

The authors acknowledge funding from the Australian Research Council (ARC) through the Special Research Centre for Multiphase Processes at the University of Newcastle (G. J. J.), the Particulate Fluids Processing Centre at the University of Melbourne (E. C. B., J. E. S.) and the ARC grants scheme.

REFERENCES

Aristoff, J. M., Lieberman, C., Chan, E. & Bush, J. W. M. 2006 Water bell and sheet instabilities. *Phys. Fluids* **18**, S10.

Bark, F. H., Wallin, H.-P., Gällstedt, M. G. & Kristiansson, L. P. 1979 Swirling water bells. *J. Fluid Mech.* **90**, 625–639.

Batchelor, G. K. 1967 *An Introduction to Fluid Dynamics*. Cambridge University Press.

Benedetto, D. & Caglioti, E. 1998 A stationary action principle for the water sheet. *Eur. J. Mech.* B/*Fluids* **17**, 770–772.

Boussinesq, J. 1869*a* Théories des expériences de Savart, sur la forme que prend une veine liquide après s'être choquée contre un plan circulaire. *C. R. Acad. Sci. Paris* **69**, 45–48.

Boussinesq, J. 1869*b* Théories des expériences de Savart, sur la forme que prend une veine liquide après s'être heurtée contre un plan circulaire (suite). *C. R. Acad. Sci. Paris* **69**, 128–131.

Brenner, M. P. & Gueyffier, D. 1999 On the bursting of viscous films. *Phys. Fluids* **11**, 737–739.

Brunet, P., Clanet, C. & Limat, L. 2004 Transonic liquid bells. *Phys. Fluids* **16**, 2668–2678.

Clanet, C. 2001 Dynamics and stability of water bells. *J. Fluid Mech.* **430**, 111–147.

Clanet, C. 2007 Waterbells and liquid sheets. *Annu. Rev. Fluid Mech.* **39**, 469–496.

Clanet, C. & Villermaux, E. 2002 Life of a smooth liquid sheet. *J. Fluid Mech.* **462**, 307–340.

Culick, F. E. C. 1960 Comments on a ruptured soap film. *J. Appl. Phys.* **31**, 1128.

Dumbleton, J. H. 1969 Effect of gravity on the shape of water bells. *J. Appl. Phys.* **40**, 3950–3954.

Engel, O. G. 1966 Crater depth in fluid impacts. *J. Appl. Phys.* **37**, 1798–1808.

Gasser, J. C. & Marty, P. 1994 Liquid sheet modelling in an electromagnetic swirl atomiser. *Eur. J. Mech.* B/*Fluids* **13**, 765–784.

Glauert, M. B. 1956 The wall jet. *J. Fluid Mech.* **1**, 625–643.

Hopwood, F. L. 1952 Water bells. *Proc. Phys. Soc.* B **65**, 2–5.

Jameson, G. J., Jenkins, C. E., Button, E. C. & Sader, J. E. 2010 Water bells formed on the underside of a horizontal plate. Part 1. Experimental investigation. *J. Fluid Mech.* **649**, 19–43.

Jeandel, X. & Dumouchel, C. 1999 Influence of viscosity on the linear stability of an annular liquid sheet. *Intl J. Heat Fluid Flow* **20**, 499–506.

Lance, G. N. & Perry, R. L. 1953 Water bells. *Proc. Phys. Soc.* B **66**, 1067–1073.

Landau, L. D. & Lifshitz, E. M. 1959 *Fluid Mechanics*, *Course of Theoretical Physics*, vol. 6. Butterworth-Heinemann.

Lin, C. C. 1945 On the stability of 2-dimensional flows. 3. stability in a viscous fluid. *Quart. Appl. Math.* **3**, 277–301.

Parlange, J.-Y. 1967 A theory of water-bells. *J. Fluid Mech.* **29**, 361–372.

Pirat, C., Mathis, C., Mishra, M. & Maïssa, P. 2006 Destabilization of a viscous film flowing down in the form of a vertical cylindrical curtain. *Phys. Rev. Lett.* **97**, 184501.

Rozhkov, A., Prunet-Foch, B. & Vignes-Adler, M. 2002 Impact of water drops on small targets. *Phys. Fluids* **14**, 3485–3501.

Savart, F. 1833*a* Mémoire sur le choc de deux veines liquides animées de mouvements directement opposés. *Ann. de Chim.* **55**, 257–310.

Savart, F. 1833*b* Mémoire sur le choc d'une veine liquide lancée contre un plan circulaire. *Ann. de Chim.* **54**, 56–87.

Taylor, G. I. 1959*a* The dynamics of thin sheets of fluid. I. Water bells. *Proc. R. Soc.* A **253**, 289–295.

Taylor, G. I. 1959*b* The dynamics of thin sheets of fluid. II. Waves on fluid sheets. *Proc. R. Soc.* A **253**, 296–312.

Taylor, G. I. 1959*c* The dynamics of thin sheets of fluid. III. Disintegration of fluid sheets. *Proc. R. Soc.* A **253**, 313–321.

Thoroddsen, S. T. 2002 The ejecta sheet generated by the impact of a drop. *J. Fluid Mech.* **451**, 373–381.

Watson, E. J. 1964 The radial spread of a liquid jet over a horizontal plane. *J. Fluid Mech.* **20**, 481–499.

Wegener, P. P. & Parlange, J.-Y. 1964 Surface tension of liquids from water bell experiments. *Zeit. Phys. Chem.* **43**, 245–259.